

Bioimage informatics

Automatic determination of NET (neutrophil extracellular traps) coverage in fluorescent microscopy images

Luis Pedro Coelho^{1,*†}, Catarina Pato², Ana Friães², Ariane Neumann³,
Maren von Köckritz-Blickwede³, Mário Ramirez² and
João André Carriço²

¹Unidade de Biofísica e Expressão Genética, Instituto de Medicina Molecular and ²Instituto de Microbiologia, Instituto de Medicina Molecular, Faculdade de Medicina, Universidade de Lisboa, Portugal and ³Department of Physiological Chemistry, University of Veterinary Medicine Hannover, Germany

*To whom correspondence should be addressed.

†Present address: European Molecular Biology Laboratory (EMBL), Heidelberg, Germany
Associate Editor: Robert Murphy

Received on July 9, 2014; revised on February 10, 2015; accepted on February 16, 2015

Abstract

Motivation: Neutrophil extracellular traps (NETs) are believed to be essential in controlling several bacterial pathogens. Quantification of NETs *in vitro* is an important tool in studies aiming to clarify the biological and chemical factors contributing to NET production, stabilization and degradation. This estimation can be performed on the basis of fluorescent microscopy images using appropriate labelings. In this context, it is desirable to automate the analysis to eliminate both the tedious process of manual annotation and possible operator-specific biases.

Results: We propose a framework for the automated determination of NET content, based on visually annotated images which are used to train a supervised machine-learning method. We derive several methods in this framework. The best results are obtained by combining these into a single prediction. The overall Q^2 of the combined method is 93%. By having two experts label part of the image set, we were able to compare the performance of the algorithms to the human interoperator variability. We find that the two operators exhibited a very high correlation on their overall assessment of the NET coverage area in the images (R^2 is 97%), although there were consistent differences in labeling at pixel level (Q^2 , which unlike R^2 does not correct for additive and multiplicative biases, was only 89%).

Availability and implementation: Open source software (under the MIT license) is available at https://github.com/luispedro/Coelho2015_NetsDetermination for both reproducibility and application to new data.

Contact: luis@luispedro.org

Supplementary information: [Supplementary data](#) are available at *Bioinformatics* online.

1 Introduction

Neutrophils are important effectors of the innate immune system in mammals, constituting the first line of defense against many microbial pathogens. Upon tissue injury and infection, neutrophils

circulating in the blood are recruited to the site of inflammation or infection, contributing to pathogen clearance through phagocytosis, production of highly toxic reactive oxygen species and release of granule proteins with antimicrobial activity (Mayadas *et al.*, 2014).

In recent years, it has been shown that some inflammatory mediators, as well as a wide range of microbes including bacteria, fungi and protozoa, can stimulate neutrophils to undergo a distinctive form of cell death designated NETosis (Yipp and Kubes, 2013). This process leads to the extracellular release of fibers of DNA associated with histones, granule proteins and peptides—neutrophil extracellular traps (NETs). These are capable of entrapping microbial pathogens and mediate their extracellular killing. It is also becoming increasingly clear that NET formation is linked to multiple neutrophil-mediated pathologies and that it is implicated in vascular injury and thrombosis (Mayadas *et al.*, 2014). Since the first identification of NETs by Brinkmann *et al.* (2004), this has become an area of active research, with many studies relying on the *in vitro* production and quantification of NETs as means to further understand the mechanisms involved in their formation, as well as their importance in pathogen clearance and in the development of multiple diseases (Buchanan *et al.*, 2006; Kessenbrock *et al.*, 2009; Marin-Esteban *et al.*, 2012; Neumann *et al.*, 2014; Wartha *et al.*, 2007; Yost *et al.*, 2009).

The spectrofluorometric quantification of NET content based on DNA release using DNA intercalating dyes has been frequently used. However, this can be confounded by the necrotic release of DNA, and by the influence of peptides present in NETs, such as LL-37, which can affect the binding of DNA to such dyes (Neumann *et al.*, 2014). The quantification of the area covered by NETs on fluorescent microscopy images is a suitable alternative, but visual quantification, besides being tedious and labor-intensive, has reproducibility problems and can present interoperator differences. In order to avoid these pitfalls, an automatic quantification method is needed. A method for the semiautomatic quantification of *in vitro* NET formation in microscopy images has been recently proposed, based on the calculation of the percentage of neutrophils that are under NETosis, corresponding mostly to a cell death program that leads to chromatin decondensation and NET formation (Brinkmann *et al.*, 2013). This method is useful for evaluating NET induction by different stimuli, but is not suitable for NET degradation experiments. In these experiments, NET production is chemically induced, so that virtually all neutrophils are activated, and the ability of degrading NETs is then evaluated based on the quantification of the DNA fibers.

Preliminary analysis showed that threshold-based methods, which Brinkmann *et al.* (2013) successfully used to detect NETs, were not able to quantify the area of the slide that was covered in NETs (which requires a more precise quantification).

We thus developed a more sophisticated method based on a supervised machine learning approach that has shown good results in other areas of bioimage informatics (Boland and Murphy, 2001; Boland *et al.*, 1998; Conrad and Gerlich, 2010; Glory and Murphy, 2007; Loo *et al.*, 2007; Nanni *et al.*, 2010) including (most similar to our work) in the segmentation of fluorescent images (Nattkemper *et al.*, 2002). These methods have even been reported to outperform human evaluation on some tasks (MacLeod *et al.*, 2010; Nattkemper *et al.*, 2003). In particular, we used a supervised learning approach whereby we learn a regression model to determine NET fraction in local regions based on numeric features computed from the pixels in that region. Finally, all the regions in an image are aggregated for a combined prediction. We present three different implementations of this generic framework based on particular choices for splitting the image into regions and different feature sets.

We also show that we can combine the outputs of the different implementations to obtain a single combined result, which outperforms all the individual predictions, as evaluated by cross validation.

Part of our data was annotated by two different experts enabling us to quantify interoperator variation. We observe that the two experts have large disagreements on a pixel-by-pixel level, with smaller disagreements on the global appreciation of the image. However, we also document a systematic bias between the two experts, highlighting the potential pitfalls of relying on human visual classification.

2 Methods

2.1 Data acquisition

Human blood-derived neutrophils were stimulated with 25 nm of phorbol 12-myristate 13-acetate (PMA) (Sigma) for 4 h to induce nearly 100% NET formation, as previously described (von Köckritz-Blickwede *et al.*, 2010). The cells were then incubated for 1 h at 37°C and 5% CO₂ with purified bacterial nucleases or with the supernatant of bacterial cultures for NET degradation. NET samples were immunostained using a mouse monoclonal anti-H2A-H2B-DNA complex (Losman *et al.*, 1992) followed by a secondary goat-anti-mouse Alexa-Fluor-488 antibody and embedded in ProlongGold + DAPI (Invitrogen) to counterstain DNA (von Köckritz-Blickwede *et al.*, 2010). Images were acquired using a Leica TCS SP5 confocal microscope with a HCX PL APO 40 × 0.75–1.25 oil immersion objective or a Zeiss LSM 710 confocal microscope with an EC Plan-Neofluar 40 × 1.30 oil immersion objective. For each preparation, randomly selected images were acquired. For most preparations, at least three images were collected.

2.2 Data labeling

NETs were labeled visually using ImageJ (Schneider *et al.*, 2012). A total of 88 fields were labeled from 30 different slides. A subset of the data (37 fields) was labeled independently by two experts, that were blinded to each other's classification. Figure 1 shows an example image, including manual segmentation by both operators.

2.3 Method evaluation

The result of our algorithm is an estimate \hat{f} of the fraction of the image area that is covered by NETs, which must be compared with the human-annotated value f . For evaluation, we used the Q^2 measure, defined by Wold (1982) as:

$$Q^2 = 1 - \frac{\sum_i (y_i - \hat{y}_i)^2}{\sum_i (y_i - \bar{y})^2}, \quad (1)$$

where \hat{y}_i is the prediction for y_i obtained by cross-validation (i.e. by evaluating a model which had not been trained using y_i), and \bar{y} is the average value across all the data. This is similar to the familiar R^2 coefficient of determination (and is referred to as cross-validated R^2 by some authors), but, unlike computing R^2 between prediction and response, it penalizes additive and multiplicative biases in the prediction.

We used a cross-validation scheme whereby all the fields from the same slide were held-out for testing, while the fields from the other slides are used for training.

2.4 Software

Software was implemented in Python, using the mahotas library for image processing and feature computation (Coelho, 2013) and scikit learn for regression (Pedregosa *et al.*, 2011). The whole dataset, code, and the learned models are available for download under the MIT license at https://github.com/luispedro/Coelho2015_Nets. A tutorial on how to apply the methods to other

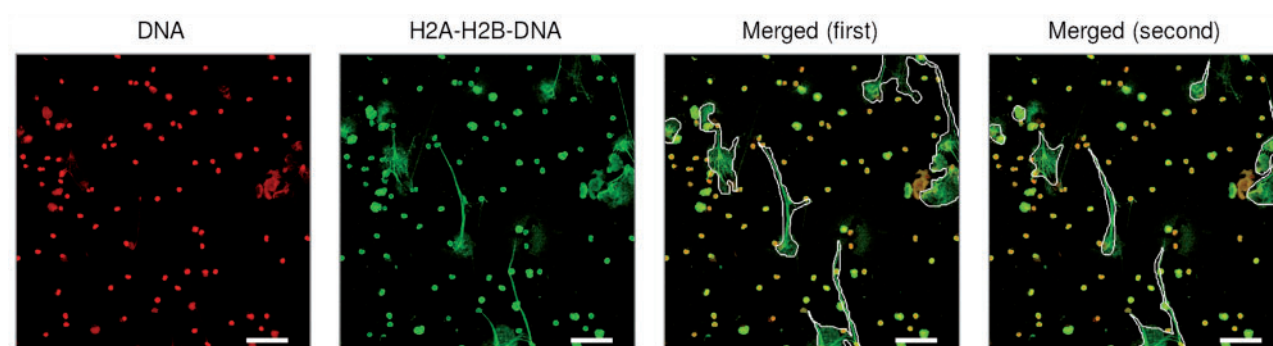


Fig. 1. Example image including comparison between human operators. Neutrophils were induced to form NETs followed by exposure to degrading agents derived from bacterial cultures. NETs were visualized using an Alexa 488-labelled antibody against H2A-H2B-DNA complexes in combination with DAPI to stain the nuclei; white lines depict human operator segmentation. The first operator marked 8.7% of the area as NETs, the second operator 5.8%. Scalebar corresponds to 50 μm . Images have been contrast stretched for publication, original data is available for download

data is available at that location as well. In the case of application to images with very similar characteristics (same tagging strategy and comparable acquisition apparatus and settings) to our own, the model may be applicable directly. For other data, it may be more appropriate to fit a new model with our software.

3 Results

3.1 A framework for automated NET quantification with three proposed implementations

We present a generic framework for NET quantification, based on human-labeled data. As input, this framework takes in a set of images, consisting of DNA and histone channels, and a human labeling of these images where regions of interest, namely NET areas, have been annotated. The framework will then produce a model which can be applied to new images to produce an estimate of the NET area in those images. We describe several methods which fall into this framework and finally we demonstrate that combining the methods obtains a better result than any single method.

The framework is illustrated in Figure 2 and consists of the following steps:

1. partition the image into regions and compute numeric descriptors (features) in each region,
2. based on the human-labeled data, learn a regression from features to estimate the fraction of area covered by NETs in each region. Estimates for regions of the same image are aggregated to form a *raw* image estimate.
3. Finally, apply a linear correction to this *raw* estimate to correct for biases in the previous steps.

The first step is motivated by the fact that NETs are present in discrete regions in the images and not throughout the image. In order to characterize these images by machine-learning methods, we compute numeric features from each region. Previous work had used similar techniques in cell segmentation problems (Chen et al., 2011; Sommer et al., 2011). We used regression to estimate the fraction of regional NET coverage, instead of classifying the regions into NET containing versus NET empty, because preliminary results showed that developing a segmentation method to obtain good agreement with manually drawn boundaries would be nontrivial and an unnecessarily hard step. Partitioning of the image can be achieved by oversegmentation or be defined geometrically (e.g. using a regular grid).

From each region, we compute a feature vector \vec{x}_i . We learn a regression function r , which returns an estimate of the local NET fraction:

$$\hat{y}_i = r(\vec{x}_i). \quad (2)$$

This function is estimated from the training data. In our implementation, we used random forest regression (Breiman, 2001) for this step (using 100 trees). This nonlinear method has the advantage of providing out-of-band estimates for the training data, which are comparable to what would have been obtained by cross-validation. These estimates are used below.

A *raw* image prediction is obtained by computing the average NET fraction over all areas. This average is weighted by the relative size of each area:

$$\hat{f}_{\text{raw}} = \frac{\sum_i \hat{y}_i s_i}{\sum_i s_i}, \quad (3)$$

where \hat{y}_i is the estimate for region i and s_i is the size of the region (in number of pixels).

The image prediction is obtained by a linear correction to the *raw* estimate

$$\hat{f}_{\text{corrected}} = \beta \hat{f}_{\text{raw}} + \alpha. \quad (4)$$

The parameters β and α were learned by least-squares minimization on the training data using the out-of-band estimates for \hat{f}_{raw} . This step corrects biases in the first regression (Wolpert, 1992) (in the results section, we present the empirical evidence for the necessity of this step). This differs from the generic stacking estimator which uses estimates from cross-validation, but when using random forests, out-of-band estimates are similar to cross-validated estimates and can be obtained at a very low computational cost (Breiman, 2001).

Finally, the fraction estimates are clipped to values between zero and one.

In what follows, we describe three different implementations of this framework, which differ in the way in which the image is broken up and the features computed.

3.1.1 Oversegmented regions

We oversegmented the Alexa channel with seeded watershed initialized with regularly spaced seeds. For each region, for both the Alexa

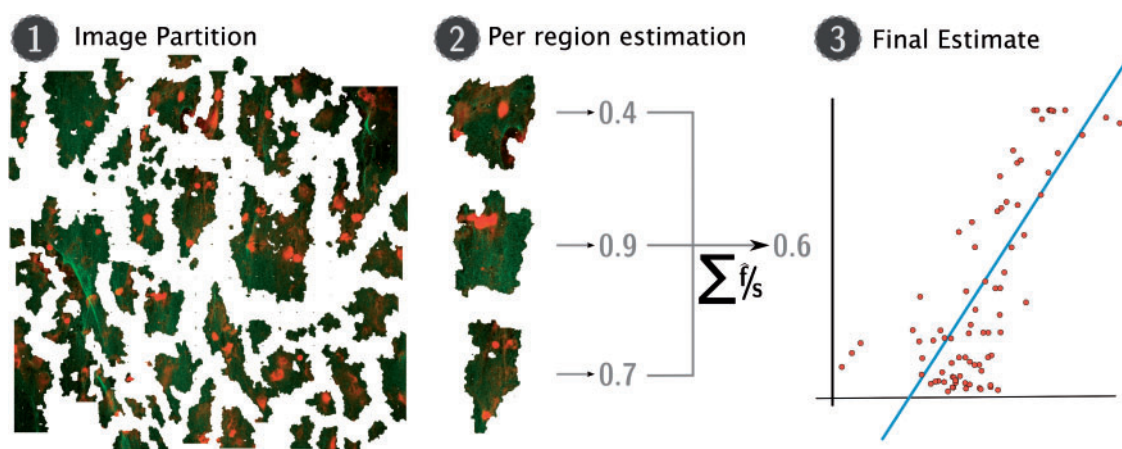


Fig. 2. Framework overview. (1) Input images are (explicitly or implicitly) partitioned into images (depicted is the result of applying the technique described in Section 3.1.1). (2) A supervised approach estimates a local fraction for each region, which is summarized to a first global estimates by a weighted average. (3) This estimate is finally corrected for biases with a linear regression

and the DAPI channel, we computed the following features (a total of 77 features were used):

1. the size of the region in pixels,
2. Haralick texture features for each of the channels (Haralick *et al.*, 1973),
3. Sobel features.
4. Haralick texture features of the Sobel filtered version of each of the channels,
5. Pearson correlation between channel intensities,
6. overlap features.

The inclusion of Sobel filtering was motivated by the observation that NETs are fibrous. Therefore, we reasoned that an edge-enhancing filter would be appropriate. The other features were included as they have been previously been shown to produce good results in similar bioimage problems (Newberg *et al.*, 2009).

Two overlap features were used: the fraction of pixels above threshold in either channel and the fraction above threshold in both channels. The mean intensity value was used as the threshold.

Regions that were smaller than 16 pixels were removed from consideration as the statistics computed on them can be unreliable due to the small number of pixels. Additionally, this step reduces the size of the input of the regression module, speeding up the process. The removed regions represent, on average, less than 4% of the total area of the image, therefore the impact of excluding these regions is small.

3.1.2 Regular sampling of filtered images (pixel regression)

Similar to what is done in Ilastik, a machine-learning based segmentation framework (Sommer *et al.*, 2011), we compute several filtered versions of the image. Then, we sample from these filtered images on a regular grid (each sample point is 8 pixels away from the next and points close to the border are discarded. This results in 3844 samples from each 512×512 image). In particular, from each channel, we computed the following filtered versions of the image (in total, 18 features are gathered at each sampling point):

1. Gaussian filtered images with different standard deviations ($\sigma = 4, 8, 12$ and 16)
2. difference of Gaussians (between $\sigma = 16$ and $\sigma = 8$)
3. Sobel filtered
4. thresholded image using both the mean pixel value and mean pixel value plus two standard deviations as thresholds

5. a version of the image where pixel values were converted to z-scores (i.e. mean subtracted and normalized by the estimated standard deviation).

From these images, pixel values were sampled in a regular grid, forming a feature vector \vec{x} . To obtain an estimate of the local NET fraction at each pixel, we considered the human-labeled NET image as a binary image and blurred it with a Gaussian filter ($\sigma = 8$ pixels). Thus, at each pixel, we have a weighted average of the NET fraction in the local region. These values are sampled at the same locations as the features to form the regression labels.

3.1.3 Dense local features

Local features have recently been shown to perform well in other bioimage informatics machine learning problems (Coelho *et al.*, 2013; Liscovitch *et al.*, 2013), including segmentation (Song *et al.*, 2013). In our work, we used dense sampling (Nowak *et al.*, 2006), whereby feature descriptors are computed in a regular grid (as above, we used an 8 pixel separation between sampling points, while discarding areas close to the image border). We compute SURF features (Bay *et al.*, 2008) computed at four different scales (namely setting 1, 2, 4 and 8 pixels as the initial scale).

As in the case of pixel regression, we associated a local NET fraction with each feature vector by smoothing the binary map with a Gaussian filter.

3.2 A combination of methods outperforms any single method

Figure 3 shows the errors committed by the individual models (errors estimated by cross-validation). We can see that the local-feature based methods show correlated errors, but this is not the case for the other methods. These data suggest that a better prediction could be obtained by combining the methods. We thus combine all methods by averaging the raw predictions of the methods before applying Equation (4).

Figure 4 summarizes the results of this study. Interestingly, the performance of all the methods is similar, with the exception of SURF features using the largest scale (8 pixels).

The results also clearly demonstrate the value of the linear correction. SURF features with a scale of 1 was the worst method before the correction, but the best (tied with pixel regression) after correction. This is explained by the fact that this model had a clear

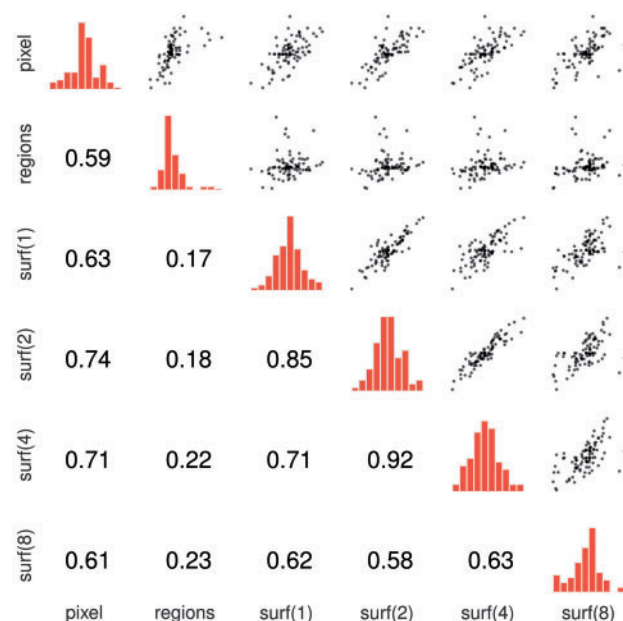


Fig. 3. Error correlations. For each cell above the diagonal, we depict a scatter plot of errors: each dot represents an image and we show the difference to the reference. If predictions exactly matched the references, all points would collapse to a single point in the centre. The diagonal shows histograms depicting the density. Below the diagonal, the Pearson correlation is displayed. The method identified as regions is described in Section 3.1.1, the one as pixel in Section 3.1.2 and the SURF approach in Section 3.1.3

multiplicative bias (see Supplementary Fig. S1). The overall Q^2 obtained by combining the methods was 93% (compared with 90% for the best performing single prediction).

In Figure 5, we plot the estimated results versus the underlying gold standard of human classification (the estimates were obtained by cross-validation). We can see that the estimates are predictive of the underlying value throughout the whole range of possible values.

3.3 Per pixel agreement between operators is low, but image-level agreement is high

Part of the data was independently labeled by two human operators (The operators were CP and AN.). Thus, we are able to quantify the amount of variance and bias in human annotation.

We found that, on a pixel-by-pixel level, the two labelings presented substantial differences. In fact, the Pearson correlation between the two binary pixel assignments was 0.68 (corresponding to 47% explained variance). Reporting explained variance of binary variables may be misleading (Abelson, 1985), but the Jaccard Index is only, on average, 0.67 (this measure ranges from 0 to 1, with 1 denoting perfect agreement). See Figure 1 for a comparison of the two operators on a single image.

However, the fraction of the area assigned to NETs by each of the operators showed a much higher correlation (R^2 is 97%). At the same time, we observed a systematic difference in labeling since one of the experts consistently reported a lower value. Reflecting this, the Q^2 measure (which penalizes for this additive error) is only 89% (see Fig. 6), slightly below the value obtained by the automated prediction.

3.4 Cross-validation per slide is a stricter measure of performance than cross-validation per field

As described above, several fields were acquired from each microscope slide. When presenting the results above, we used a

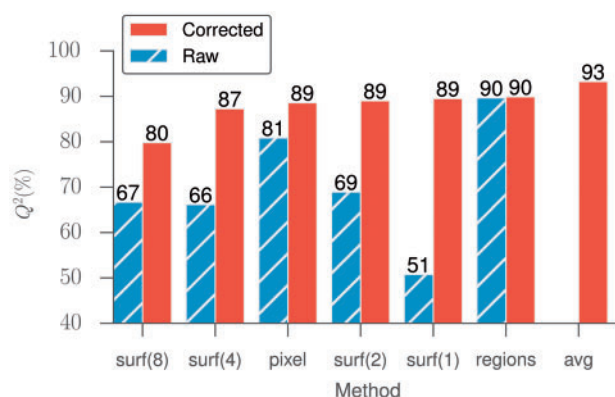


Fig. 4. Results for all of the methods. Methods are ordered by the quality of their corrected predictions

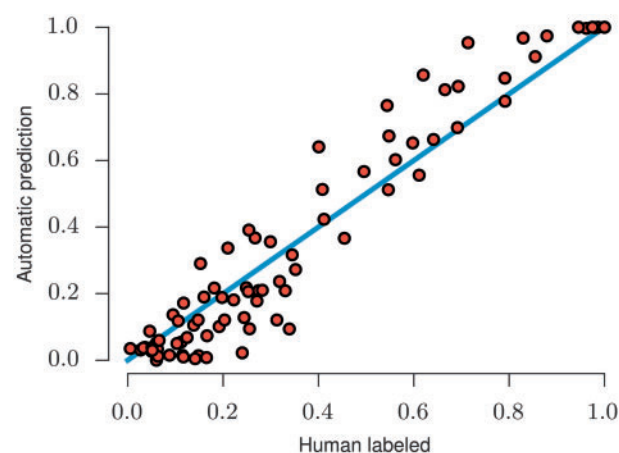


Fig. 5. Final combined prediction. Each dot represents an image, plotting the underlying gold standard on the horizontal axis and the cross-validated prediction on the vertical axis. Prediction were obtained by cross-validation, i.e. the NET fraction of each image is estimated from a model which was trained on data *not including* that particular image nor any image from the same slide

cross-validation scheme whereby we held out a slide at a time for testing and trained on the rest of the data. To support our choice, we also considered an alternative schedule whereby a single field is left out at a time. Thus, each field is evaluated by a model which is obtained from training data which includes other fields from the same slide.

The results show that such approach would lead to over-inflated performance measures. For instance, when the combined method is evaluated in this manner, we obtain a Q^2 value of 95% (higher than the 93% we obtained in stricter testing approach). Similarly small but positive differences are observed when evaluating all the individual methods (see Supplementary Table S1).

4 Discussion

We present a framework for automated quantification of NET area in fluorescent microscopy images. Based on this generic framework, we implemented three specific methods. Follow-up work may make different choices of implementation and arrive at different methods. The use of different feature sets, different oversegmentation methods or a different regression methodology are all potential avenues to

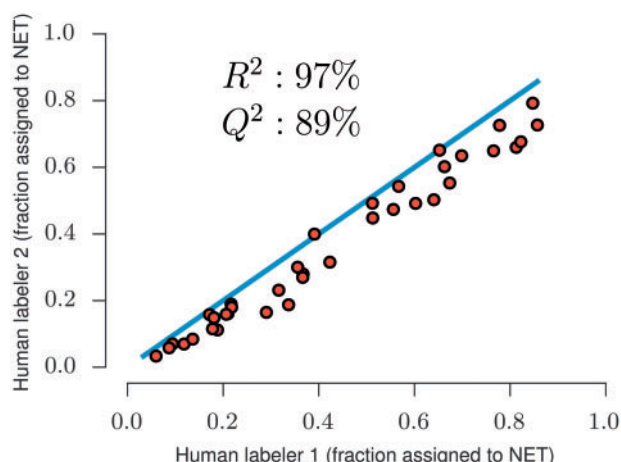


Fig. 6. Comparison between different human operators. Each circle represents a labeled image, the solid line shows the diagonal (hypothetical perfect agreement)

explore whilst staying within the generic framework we propose in this work.

The final output of our method is a single fraction measurement which does not directly relate back to pixel assignments. While the ideal method would compute a perfect segmentation, from which the NET fraction would be trivially estimated, it is not necessary to obtain this segmented image in order to solve a biologically relevant question. A single fraction estimate can provide enough information for the user. This is in accordance with work in computer vision which had previously shown that to get accurate cell counts, it is not necessary to completely segment individual cells (Lempitsky and Zisserman, 2010).

The fact that we only aimed to obtain single overall estimate from each image, instead of pixel assignments, allowed us to build a stacked estimator from the different methods to obtain a final prediction, even though these do not share the same partitions of the image (Wolpert, 1992). On our data, the gains from combining different predictions is at least partially explained by the fact that the errors of the different methods are only weakly correlated.

Previous work by Coelho *et al.* (2013) had demonstrated the need for careful delineation of data for cross-validation in the context of subcellular location determination. In this work, we reinforce the point in a different context, namely automated determination of NET content, by demonstrating that when different images from the same sample are used for training and testing, the measured performance is increased relative to validation from data from different samples. This is likely due to overfitting to match very particular aspects of each slide as opposed to generalizable features of NETs.

We also empirically investigated and measured the agreement between different human evaluators. The results require a nuanced interpretation. The pixel-level agreement is very low, but the two experts have very high correlation in their evaluations of the images. This is another instance where pixel-level measures are misleading, a phenomenon we and others had already investigated in the case of nuclear segmentation (Coelho *et al.*, 2009; Yang-Mao *et al.*, 2008). The general conclusion is that for evaluation of automated techniques, the evaluation measure should be as close as possible to the underlying biological goal (in our case, the fraction of the sample covered by NETs) and not an intermediate result (the exact locations of such areas).

The high correlation between human operators was hiding a systematic bias in quantitative results. One of the operators systematically reported a lower value. The automated method was more consistent with the data that it was trained on, resulting in a lower Q^2 value.

Although the samples were prepared using the same protocol, the image acquisition equipment and parameters were not the same (see Section 2). Despite these differences, the proposed algorithm was able to classify equally well images obtained with either condition, suggesting that it is insensitive to any potential specificities introduced.

The automated method has a lower cost, perfect reproducibility, and results in a faster processing of the images than human annotation. Automated analysis opens up the possibility of multistudy comparisons by consortia of independent laboratories, which can be trained with their data and assessed by the method proposed. This can result in more robust training sets that can accommodate more significant differences in sample preparation protocol and data acquisition conditions. In its current form, the robustness of the proposed automated process, when combined with automated image acquisition, can facilitate the analysis in a single laboratory of numbers of fields and samples that would be prohibitive using manual annotation. Such large-scale analysis will certainly improve confidence in the determination of NET area, providing more accurate and reproducible analyses than is currently available from human annotation. Our data is available for others in the community.

Funding

L.P.C. was supported by Fundação para a Ciência e a Tecnologia (grant PTDC/SAU-GMG/115652/2008). M.v.K.-B. was supported in part by DFG grant KO 3552/4-1. A.N. was supported by a fellowship of the Akademie für Tiergesundheit (AfT) and the PhD programme 'Animal and Zoonotic Infections' of the University of Veterinary Medicine Hannover, Germany. A.F. received a Short-Term Fellowship 2011 by the Federation of European Biochemical Societies (FEBS) and an ESCMID Travel Grant for Training in a Foreign Institution 2011 by the European Society of Clinical Microbiology and Infectious Diseases (ESCMID).

Conflict of Interest: none declared.

References

- Abelson, R.P. (1985) A variance explanation paradox: when a little is a lot. *Psychol. Bull.*, **97**, 129–133.
- Bay, H. *et al.* (2008) Speeded-up robust features (SURF). *Comput. Vis. Image Understand.*, **110**, 346–359.
- Boland, M.V. and Murphy, R.F. (2001) A neural network classifier capable of recognizing the patterns of all major subcellular structures in fluorescence microscope images of hela cells. *Bioinformatics*, **17**, 1213–1223.
- Boland, M.V. *et al.* (1998) Automated recognition of patterns characteristic of subcellular structures in fluorescence microscopy images. *Cytometry*, **33**, 366–375.
- Breiman, L. (2001). Random forests. *Mach. Learn.*, **45**, 5–32.
- Brinkmann, V. *et al.* (2004) Neutrophil extracellular traps kill bacteria. *Science*, **303**, 1532–1535.
- Brinkmann, V. *et al.* (2013) Automatic quantification of in vitro net formation. *Front. Immunol.*, **3**, doi: 10.3389/fimmu.2012.
- Buchanan, J.T. *et al.* (2006) DNase expression allows the pathogen group a streptococcus to escape killing in neutrophil extracellular traps. *Curr. Biol.*, **16**, 396–400.
- Chen, C. *et al.* (2011) A pixel classification system for segmenting biomedical images using intensity neighborhoods and dimension reduction. In: *Biomedical Imaging: From Nano to Macro, 2011 IEEE International Symposium on*, pp. 1649–1652.

- Coelho,L.P. (2013) Mahotas: Open source software for scriptable computer vision. *J. Open Res. Softw.*, 1.
- Coelho,L.P. et al. (2009) Nuclear segmentation in microscope cell images: a hand-segmented dataset and comparison of algorithms. In: *IEEE International Symposium on Biomedical Imaging: From Nano to Macro*, 2009. ISBI'09, pp. 518–521.
- Coelho,L.P. et al. (2013) Determining the subcellular location of new proteins from microscope images using local features. *Bioinformatics*, 29, 2343–2349.
- Conrad,C. and Gerlich,D.W. (2010) Automated microscopy for high-content rnai screening. *J. Cell Biol.*, 188, 453–461.
- Glory,E. and Murphy,R.F. (2007) Automated subcellular location determination and high-throughput microscopy. *Dev. Cell*, 12, 7–16.
- Haralick,R.M. et al. (1973) Textural features for image classification. *IEEE Trans. Syst. Man Cybernet.*, 3, 610–621.
- Kessenbrock,K. et al. (2009) Netting neutrophils in autoimmune small-vessel vasculitis. *Nat. Med.*, 15, 623–625.
- Lempitsky,V.S. and Zisserman,A. (2010) Learning to count objects in images. In: *NIPS*, vol. 1, p. 2.
- Liscovitch,N. et al. (2013) FuncISH: learning a functional representation of neural ish images. *Bioinformatics*, 29, i36–i43.
- Loo,L.-H. et al. (2007) Image-based multivariate profiling of drug responses from single cells. *Nat. Methods*, 4, 445–453.
- Losman,M.J. et al. (1992) Monoclonal autoantibodies to subnucleosomes from a mrl/mp (-)/+ mouse. oligoclonality of the antibody response and recognition of a determinant composed of histones h2a, h2b, and dna. *J. Immunol.*, 148, 1561–1569.
- MacLeod,N. et al. (2010) Time to automate identification. *Nature*, 467, 154–155.
- Marin-Esteban,V. et al. (2012) Afa/dr diffusely adhering escherichia coli strain c1845 induces neutrophil extracellular traps that kill bacteria and damage human enterocyte-like cells. *Infect. Immun.*, 80, 1891–1899.
- Mayadas,T.N. et al. (2014) The multifaceted functions of neutrophils. *Annu. Rev. Pathol.*, 9, 181–218.
- Nanni,L. et al. (2010) Local binary patterns variants as texture descriptors for medical image analysis. *Artif. Intell. Med.*, 49, 117–125.
- Nattkemper,T.W. et al. (2002) A neural network architecture for automatic segmentation of fluorescence micrographs. *Neurocomputing*, 48, 357–367.
- Nattkemper,T.W. et al. (2003) Human vs. machine: evaluation of fluorescence micrographs. *Comput. Biol. Med.*, 33, 31–43.
- Neumann,A. et al. (2014) Novel role of the antimicrobial peptide ll-37 in the protection of neutrophil extracellular traps against degradation by bacterial nucleases. *J. Innate Immun.*
- Newberg,J.Y. et al. (2009) Automated analysis of human protein atlas immunofluorescence images. In: *Proceedings IEEE International Symposium on Biomedical Imaging: From Nano to Macro*, vol. 5193229, pp. 1023–1026.
- Nowak,E. et al. (2006) Sampling strategies for bag-of-features image classification. In: *Computer Vision–ECCV 2006*. Springer, Berlin, pp. 490–503.
- Pedregosa,F. et al. (2011) Scikit-learn: machine learning in Python. *J. Mach. Learn. Res.*, 12, 2825–2830.
- Schneider,C.A. et al. (2012) NIH image to ImageJ: 25 years of image analysis. *Nat. Methods*, 9, 671–675.
- Sommer,C. et al. (2011) ilastik: Interactive learning and segmentation toolkit. In: *IEEE International Symposium on Biomedical Imaging: From Nano to Macro*, pp. 230–233.
- Song,Y. et al. (2013) Region-based progressive localization of cell nuclei in microscopic images with data adaptive modeling. *BMC Bioinformatics*, 14, 173.
- von Köckritz-Blickwede,M. et al. (2010) Visualization and functional evaluation of phagocyte extracellular traps. *Methods Microbiol.*, 37, 139–160.
- Wartha,F. et al. (2007) Capsule and d-alanylated lipoteichoic acids protect streptococcus pneumoniae against neutrophil extracellular traps. *Cell. Microbiol.*, 9, 1162–1171.
- Wold,H. (1982) Soft modeling: the basic design and some extensions. In: *Systems Under Indirect Observation*, vol. 2, pp. 589–591.
- Wolpert,D.H. (1992) Stacked generalization. *Neural Netw.*, 5, 241–259.
- Yang-Mao,S.-F. et al. (2008) Edge enhancement nucleus and cytoplasm contour detector of cervical smear images. *IEEE Trans. Syst. Man Cybernet. Part B*, 38, 353–366.
- Yipp,B.G. and Kubes,P. (2013) Netosis: how vital is it? *Blood*, 122, 2784–2794.
- Yost,C.C. et al. (2009) Impaired neutrophil extracellular trap (NET) formation: a novel innate immune deficiency of human neonates. *Blood*, 113, 6419–6427.